



Cite as
Nano-Micro Lett.
(2024) 16:222

Received: 19 February 2024
Accepted: 14 May 2024
Published online: 17 June 2024
© The Author(s) 2024

Tree-Inspired Structurally Graded Aerogel with Synergistic Water, Salt, and Thermal Transport for High-Salinity Solar-Powered Evaporation

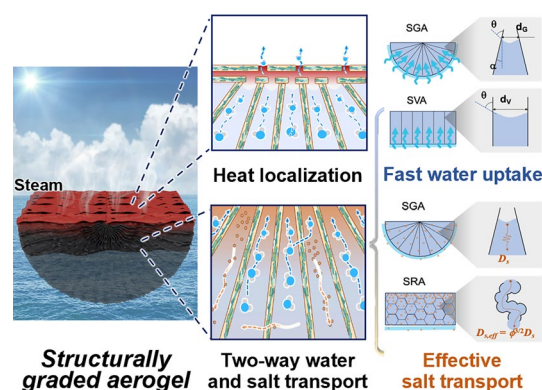
Xiaomeng Zhao¹, Heng Zhang¹, Kit-Ying Chan^{1,3}, Xinyue Huang¹, Yunfei Yang¹,
Xi Shen^{1,2,3} ✉

HIGHLIGHTS

- Inspired by transport system in trees, a two-way water and salt transport mechanism is realized in a structurally graded aerogel, enabling simultaneous fast water uptake and salt rejection.
- The horizontally aligned pore channels near the surface achieve excellent heat localization by maximizing solar absorption and minimizing heat loss.
- The integrated water, salt, and thermal transports impart an impressive evaporation rate of $1.94 \text{ kg m}^{-2} \text{ h}^{-1}$ in a 20 wt% NaCl solution for 8 h without salt accumulation.

ABSTRACT Solar-powered interfacial evaporation is an energy-efficient solution for water scarcity. It requires solar absorbers to facilitate upward water transport and limit the heat to the surface for efficient evaporation. Furthermore, downward salt ion transport is also desired to prevent salt accumulation. However, achieving simultaneously fast water uptake, downward salt transport, and heat localization is challenging due to highly coupled water, mass, and thermal transport. Here, we develop a structurally graded aerogel inspired by tree transport systems to collectively optimize water, salt, and thermal transport. The arched aerogel features root-like, fan-shaped microchannels for rapid water uptake and downward salt diffusion, and horizontally aligned pores near the surface for heat localization through maximizing solar absorption and minimizing conductive heat loss. These structural characteristics gave rise to consistent evaporation rates of $2.09 \text{ kg m}^{-2} \text{ h}^{-1}$ under one-sun illumination in a 3.5 wt% NaCl solution for 7 days without degradation. Even in a high-salinity solution of 20 wt% NaCl, the evaporation rates maintained stable at $1.94 \text{ kg m}^{-2} \text{ h}^{-1}$ for 8 h without salt crystal formation. This work offers a novel microstructural design to address the complex interplay of water, salt, and thermal transport.

KEYWORDS Composite aerogel; Graded structure; Solar-powered evaporation; Thermal insulation; Salt rejection



✉ Xi Shen, xi.shen@polyu.edu.hk

¹ Department of Aeronautical and Aviation Engineering, The Hong Kong Polytechnic University, Hung Hom, Kowloon, Hong Kong SAR, People's Republic of China

² Research Institute for Sports Science and Technology, The Hong Kong Polytechnic University, Hung Hom, Kowloon, Hong Kong SAR, People's Republic of China

³ Research Institute for Advanced Manufacturing, The Hong Kong Polytechnic University, Hung Hom, Kowloon, Hong Kong SAR, People's Republic of China



1 Introduction

Water scarcity has become an urgent global challenge requiring sustainable and environmentally friendly solutions [1–3]. Solar-powered evaporation, leveraging solar energy to evaporate seawater or wastewater for conversion into clean and potable water, is a highly promising technology because of its energy-saving potential with renewable solar energy as the sole energy source [4]. This technology relies on solar absorbers to capture incident sunlight and convert it into highly concentrated thermal energy confined at the water–air interface where highly efficient water evaporation occurs [5]. Three-dimensional (3D) solar absorbers in the form of fabrics [6, 7], aerogels [8–11], and hydrogels [12–14] have been developed from a range of photothermal materials such as carbon nanotubes (CNTs), graphene, and MXene. These materials have been designed as standalone evaporators serving on water surfaces to enable solar absorption, water transport, and heat localization through engineering their highly porous structures, contributing to high solar-to-vapor energy conversion efficiency of over 90% and evaporation rates close to the theoretical limit ($\sim 1.47 \text{ kg m}^{-2} \text{ h}^{-1}$) under standard one-sun illumination, promising for high-yield desalination and wastewater treatment applications [12]. Despite these promising properties, one major drawback of 3D solar absorbers is the salt accumulation especially under high-salinity situations. During evaporation of high-salinity brine or high-concentration wastewater, salts, minerals, and impurities precipitated from the solution and accumulated on the evaporation surface due to supersaturation of the surface solution [15, 16], reducing the solar absorption and impeding the water transport which in turn reduced the overall evaporation performance [17–19]. To avoid salt accumulation, smart structural designs such as evaporators with dual evaporation modes have been proposed to redissolve the salts by self-rotating [20]. Although accumulated salts could be removed by subsequent flushing [21], dissolved by self-cleaning [22], or collected by gravity-assisted methods [23], these time-consuming steps were deleterious to continuous operations. Localizing salts on evaporation surface is another effective strategy, which can be realized by controlling the brine transport or non-contact design [24], leading to zero liquid discharge during the evaporation process [25]. While non-contact evaporators [26–28] avoided salt crystal formation on their surfaces because of the physical

separation from seawater, such separation in turn gave rise to low energy conversion efficiency and thus relatively low evaporation rates ($\sim 1.3 \text{ kg m}^{-2} \text{ h}^{-1}$). Circumventing salt accumulation on 3D evaporators without impairing their rapid water transport and heat localization remains a significant challenge for practical desalination under high-salinity conditions, primarily due to highly coupled water, salt, and thermal transport in the evaporators.

Several strategies have been developed to tackle the salt accumulation issue through decoupling water, salt, and thermal transports, including Janus surface design [29, 30], ion rejection [17, 31, 32], salt localization [23, 33], and diffusive/convective backflow [12, 34–37]. The Janus design stacked hydrophobic photothermal layer and hydrophilic water absorbing layer in tandem to prevent brine transport onto the photothermal surface. Nevertheless, the separating functions of water transport and solar absorption discourage fast water transport to the surface, not ideal for a high evaporation rate. Salt localization involved the directional transport of brine to a confined location for crystallization. The heat loss associated with brine transport was rather significant, undesirable for a high energy efficiency. Ion rejection encompassed the incorporation of ion-selective groups or species in hydrogels to manipulate the transport of salt ions through ionic interactions. Although salt crystal formation was completely eliminated through the ion rejection mechanism, water transport channels, solar absorption layers, and thermal insulation design were implemented separately to allow effective evaporation. All in all, these approaches decoupled thermal, salt, and water transports by integrating different functional constituents to achieve simultaneous heat localization, fast water delivery, and salt rejection, but inevitably complicated the whole system because of separated components for individual functions.

Compared to the above, diffusive/convective backflow is a promising strategy to use a single structure for salt rejection without compromising heat localization and water transport. The principle involved diffusive or convective flows driven by salt concentration gradient to prevent surface solution from reaching saturation [38]. Proper structural design is essential to ensure fast downward salt ion diffusion or convection, avoiding salt crystal precipitation at the heating surface [19]. Commonly, solar absorbers have been engineered with vertically aligned pores using techniques such as freeze-casting [39], serving as direct conduits for water

uptake and fast salt ion diffusion [12, 35, 36]. The diffusion could be further enhanced by using macroscopic channels [40, 41]. For example, through-the-thickness channels of millimeter-scale diameters were drilled into a wood panel, inducing salt ion transport from micron-size xylem channels to millimeter-size channels for enhanced salt rejection [41]. However, the macroscopic channels inadvertently accelerated heat conduction through water and vertical pore walls, resulting in increased heat loss and reduced energy efficiency [42, 43]. Further tuning the dimensions of macroscopic channels led to engineered fluidic flow with passive convection driven by salinity gradients [44]. Leveraging the substantial disparity between the low salt diffusivity in water and the high thermal diffusivity of water, an optimized channel size was attained to enable salt rejection through convective flow while maintaining the heat transport in a diffusive regime to minimize heat loss, ultimately achieving a high efficiency of over 80% in a high-salinity solution of 20 wt%.

Despite these ameliorating efforts in balancing salt and thermal transport in vertical pores, the energy efficiency and evaporation rate are still not satisfactory due to inevitable downward thermal transport through solid pore walls and high-thermal-conductivity water. To reduce the downward thermal conduction, horizontal pores were preferred over vertical ones because of the low thermal conductivity (TC) across the pore alignment direction [45–47]. This conflicting requirement makes it challenging to achieve excellent thermal localization concurrently with water transport and salt rejection, necessitating complex bidirectional structural features to reach a tradeoff. Attempt has been made to develop a feather-like anisotropic hierarchical structure with longitudinal struts and transverse ligaments [48], efficiently delivering water to the evaporating surface while providing exceptional transverse insulation. A vertical radiant structure was also designed to allow salt diffusion through vertical pores at the center while reducing the heat conduction through radially arranged horizontal vessels, striking a balance between thermal localization and salt resistance [49]. While the bidirectional pores allow fast downward salt diffusion and good insulation, the upward water transport was not optimized simultaneously. It is challenging to realize fast upward water transport for evaporation and downward ion transport for salt rejection at the same time while also maintaining good thermal insulation for high energy efficiency because of highly coupled water, salt, and thermal transport.

In this study, we propose an integrated strategy to synergistically optimize water, salt, and thermal transport through developing a structurally graded aerogel (SGA) for two-way water and salt transport as well as heat localization. The multiscale structures of SGA were designed to mimic the entire transport system of trees (Fig. 1). The fan-shaped, tapered channels delivered a two-way water and salt transport mechanism for fast water uptake and downward salt diffusion. Simultaneously, the horizontally aligned surface pore channels achieved excellent heat localization through maximizing the solar absorption and minimizing thermal emission and conduction. The co-optimization of water, salt, and heat transport gave rise to consistent evaporation rates averaging at $2.09 \text{ kg m}^{-2} \text{ h}^{-1}$ under one-sun illumination in a 3.5 wt% NaCl solution for 7 days without degradation. Even for a high-salinity solution of 20 wt% NaCl, the evaporation rates maintained stable at $1.94 \text{ kg m}^{-2} \text{ h}^{-1}$ for 8 h without salt crystal formation. These results underscore the significant potential of SGA for solar-powered desalination and purification of high-salinity brines or high-concentration wastewaters.

2 Experimental Section

2.1 Materials

Polyvinyl alcohol (PVA, 99 + % hydrolyzed, molecular weight of 146,000 to 186,000) was supplied by Sigma-Aldrich. Graphene oxide (GO) solution (2 mg mL^{-1}) and CNTs (> 95%, carboxyl content: 3.86%) were purchased from XFNANO, China. Sodium chloride (NaCl, 99.5%) was supplied by Aladdin Chemistry Co. Ltd. All the materials and chemicals were used without any treatment. Seawater was taken from the Victoria Harbour of South China Sea near the Hong Kong Polytechnic University.

2.2 Fabrication of SGA

First, 10 g PVA powders were dissolved in 100 g deionized (DI) water at 130°C for 2 h. Then, the GO solution and CNT powders were mixed at a ratio of 3:7 and stirred continuously for 3 h followed by ultrasonication for 0.5 h at room temperature until a uniform GO-CNT dispersion was obtained. Subsequently, the required amount of PVA solution was added to the above GO-CNT dispersion, and the

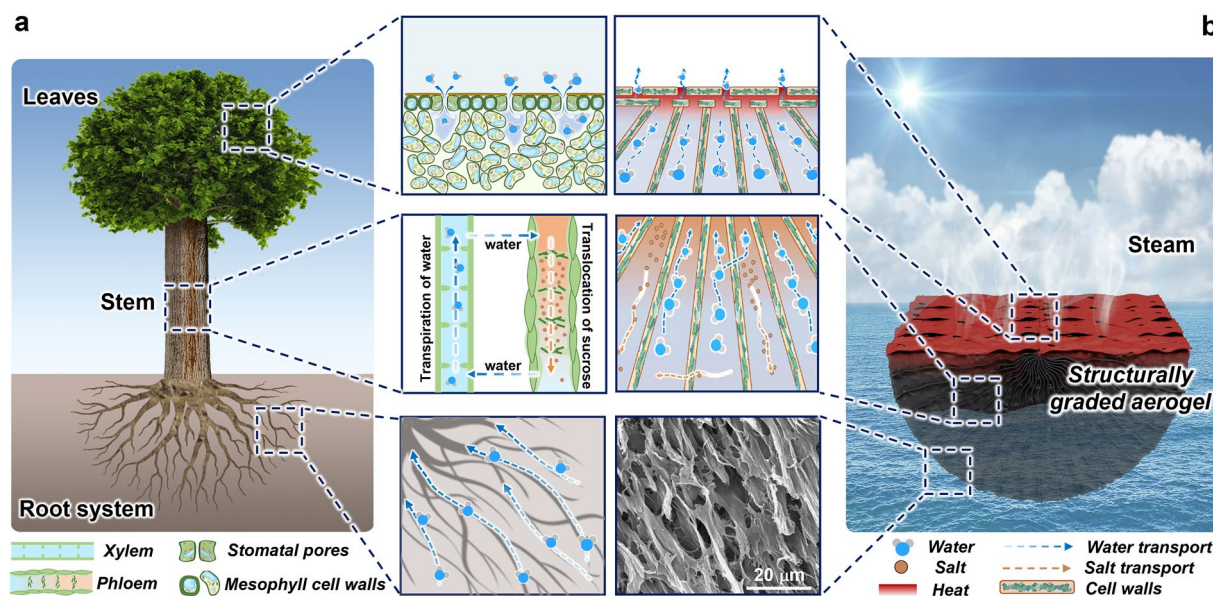


Fig. 1 Biomimetic design of SGA. Schematics showing the water and mass transport mechanisms in **a** trees and **b** SGA

mixture was continuously stirred at room temperature for 3 h to obtain a GO-CNT/PVA mixture solution. SGA was fabricated by radial freeze-casting followed by freeze-drying (as shown in Fig. 2a later). The GO-CNT/PVA mixture solution was poured into a copper mold which was partially immersed in liquid nitrogen bath. After the solution was frozen completely, the sample was freeze-dried in a freeze-dryer (Scientz-10n) at 5 Pa for 36 h. For comparison, structurally vertical aerogel (SVA) and structurally random aerogel (SRA) were also prepared with the same steps except that GO-CNT/PVA mixture solution was freeze-cast vertically using a bottom copper cold source and randomly in a refrigerator, respectively.

2.3 Characterization

The sample morphologies and microstructures were observed using the scanning electron microscopy (SEM, Tescan VEGA3). The solar absorption spectra were measured using a ultraviolet–visible–near infrared (UV–vis–NIR) spectrophotometer (3700DUV, Shimadzu) from 250 to 2500 nm with an integrating sphere. The solar absorption (A) was calculated by $A = 1 - R - T$, where R and T are the reflection and transmission, respectively. The TCs of different aerogels were measured based on a transient plane heat

source method (Hot Disk TPS2500S). The IR images were taken using an IR camera (FLIR-B256V, Guide Sensmart). Raman spectroscopy (InVia, Renishaw, 514 nm laser) was used to identify the presence of carbon nanomaterials in the aerogels. The real-time temperature distributions were measured using thermocouples and recorded by a data logger (CENTER 309). Ion concentrations were measured using an inductively coupled plasma optical emission spectrometer (ICP-OES, Agilent 5110). Tensile and compressive properties were measured on a Shimadzu AGS-X Tester.

2.4 Solar-Powered Water Evaporation Experiments

To systematically compare the evaporation performance of aerogels with different structures, a series of water evaporation tests were conducted at a relative humidity of 50% and ambient temperature. The aerogel sample was floated on the water surface in a glass beaker with the surrounding water being covered with a polyethylene foam to avoid the direct evaporation of bulk water. The sample was continuously illuminated by a solar simulator (CEL-S500/350) for 1 h under various solar intensities measured by a solar power meter (TES-1333R). The mass loss of water was recorded in real

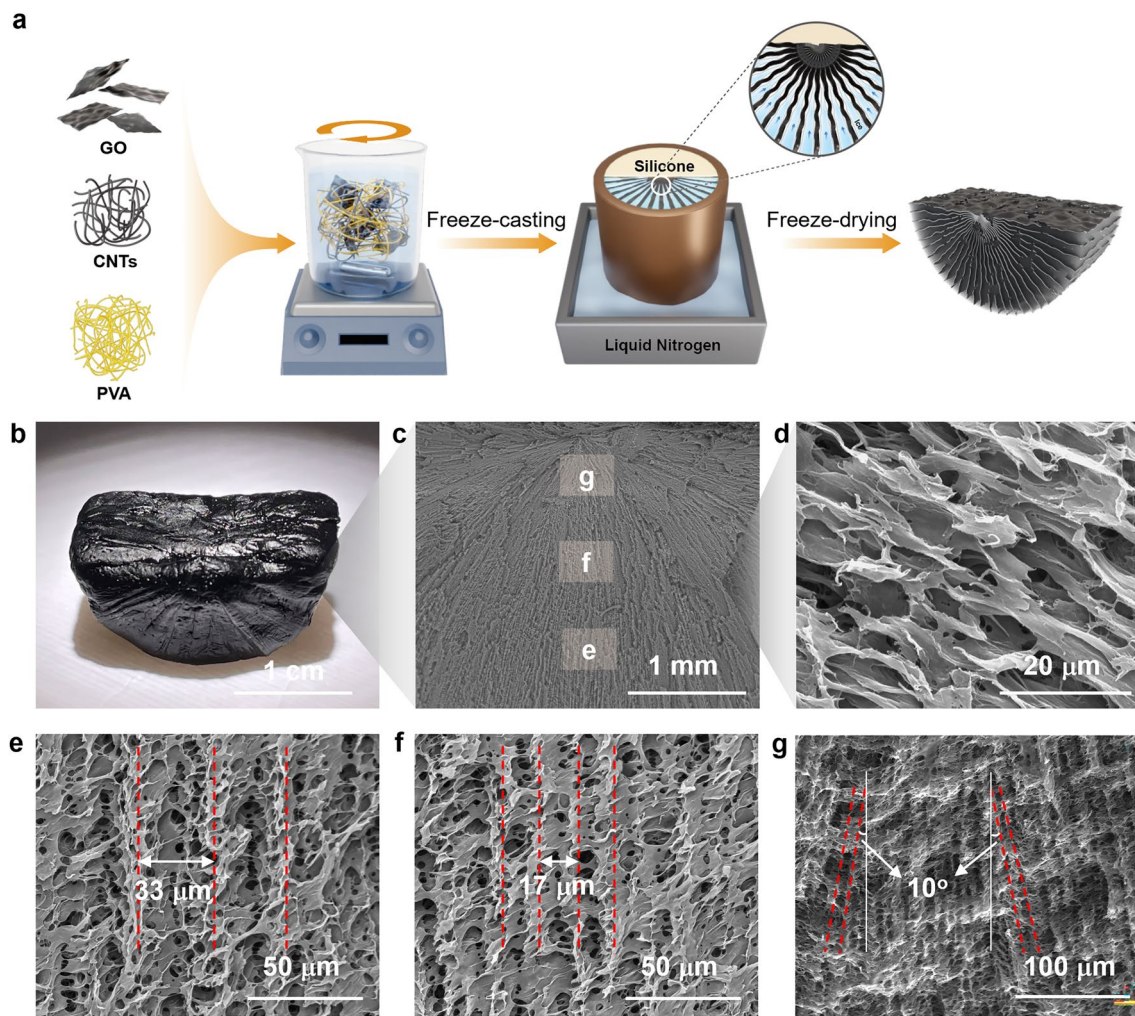


Fig. 2 Fabrication and structural characteristics of SGA. **a** Schematic of fabrication of SGA with fan-shaped gradient structures. **b** Photograph of SGA showing its black appearance and hull-like arched bottom. SEM images showing **c** the fan-like cell walls and **d** fine-root-like secondary ligaments of SGA. **e–g** High-magnification SEM images showing detailed channel widths at different positions marked in (c)

time by an electronic balance (FA2004, 0.1 mg). At least two independent measurements were carried out for each test.

2.5 Salinity Measurements

The salinity was measured using a digital refractometer (DLX-ARHT028). A small amount of brine was carefully collected from the water–air interface or the bulk brine using a glass point capillary tube with an inner diameter of 0.9 mm and length of 100 mm. The collected brine was dripped onto the lens of the digital refractometer for reading the salinity.

3 Results and Discussion

3.1 Biomimetic Design of SGA

Trees are natural solar-driven evaporators capable of passively transporting water from roots to leaves via their stems [50]. Tree roots play a dominant role in absorbing water from the soil, which is then transported up through stems to leaves for photosynthesis. Stems are also responsible for transferring sugars made in the leaves during photosynthesis downwards to other parts of the tree.

Meanwhile, the water evaporates from leaves through cell wall pores under sunlight, driving the continuous water uptake through capillary forces. The spontaneous, solar-driven mass transport can be attributed to several unique structural features in roots, stems and leaves, as shown in Fig. 1a [45]. First, roots grow radially in all directions to maximize the contact area and thus accessible water in the soil. Moreover, fine roots at the tips are covered by root hairs to increase the surface area for water absorption. Second, the absorbed water is passively transported upwards through the xylem driven by the water pressure gradient owing to water evaporation from the leaves. Meanwhile, sugars produced from leaves create a concentration gradient in the phloem, driving the downward transportation of sugars from leaves to roots by diffusion. Third, leaves with large surface areas are capable of absorbing sunlight for transpiration, where water evaporates from the mesophyll cell walls through the stomatal pores on the leaf surfaces, increasing the surface tension on the water menisci and thus pumping the water up in the xylem channels. While evaporators with vertical channels mimicking the xylem vessels for water transport have been well developed [41, 51–53], little effort has been made to fully imitate the entire structures and mechanisms of trees for synergistic upward water transport and downward salt transport for simultaneous water evaporation and salt rejection. Here, we designed and fabricated an SGA to mimic the intricate transport system in trees (Fig. 1b). The SGA was made from a mixture of GO, CNTs, and PVA to endow both excellent sunlight absorption and hydrophilicity [54]. The SGA had a boat-like, arched bottom with fan-shaped walls radiating from the top to bottom, resembling the tree root structure which gave rise to a better stability and larger water contact area than a flat surface for water absorption. Similar to fine roots, the whisker-like struts grown from the main cell walls in SGA further improved the surface area for water absorption. Meanwhile, the pore channels formed between radiating cell walls tapered down to the evaporating surface, facilitating fast upward water transport driven by water potential gradient and downward salt diffusion induced by salt concentration gradient, mimicking the two-way water and mass transport mechanism in the xylem and phloem. Furthermore, the flat evaporating surface formed by horizontal cell walls served the same function as leaves, providing large surface areas for sunlight absorption and numerous pores for vapor escape. The

horizontally aligned pores near the surface also limited the downward heat conduction [55, 56], beneficial to a low heat loss for high energy efficiency.

3.2 Fabrication and Structural Characteristics of SGA

To construct the fan-shaped microstructure, the SGA was fabricated from a mixture of GO, CNT and PVA solution by a freeze-casting technique using a custom-made hollow cylindrical copper mold as the cold source (Fig. 2a). Half of the mold and the bottom were filled with low-thermal-conductivity polydimethylsiloxane (PDMS), generating a temperature gradient from peripherals to the center to force the radial growth of ice crystals (Fig. S1, detailed fabrication can be found in Experimental Section) [57, 58]. The freeze-casting technique could produce SGA of different sizes by using molds of different sizes (Fig. S2a). It was also adaptable to fabricate aerogels with other shapes such as that with a hemispherical bottom by using a half-spherical mold (Fig. S3a). The concentrations of carbon nanofillers and PVA were first optimized by changing their weight ratios and an optimized ratio of 0.05 was used in the subsequent discussion (see Supplementary Note S1 and Figs. S4 to S6 for details). Figure 2b–g shows the multiscale structural features of SGA. The SGA appeared black thanks to the presence of GO and CNT fillers as confirmed by the Raman spectra (Fig. S7), beneficial for sunlight absorption. Unlike the rectangular shape in most floating evaporators, the SGA featured a cylindrical bottom resembling the hull of a boat (Fig. 2b), essential to buoyant stability in practical operations (Fig. S8). SGA with different sizes also showed good buoyant stability (Fig. S2b). Although the hemispherical aerogel could be floated more stable than SGA because of a higher degree of stability in any in-plane directions, its evaporation performance was inferior to SGA (Fig. S3b). The SEM image of SGA (Fig. 2c) indicates fan-shaped cell walls radiating from top to peripheries because of directional ice crystal growths, much like the spreading roots to enhance the accessible area for absorbing water. Moreover, numerous secondary ligaments were observed in addition to the main cell walls (Fig. 2d), functioning the same as fine roots to increase the surface area for water absorption.

At higher magnifications, the widths of the channels between radiating cell walls gradually tapered from $\sim 33 \mu\text{m}$ (Fig. 2e) at the bottom to $\sim 17 \mu\text{m}$ (Fig. 2f) near the center, ultimately narrowing down to only $\sim 9 \mu\text{m}$ at the top (Fig. 2g). These gradient channels imparted a high capillary pressure at the water–air interface and a salt concentration gradient from top to bottom, facilitating upward water and downward salt transport mechanism similar to that of xylem and phloem. The pore channels near the surface aligned horizontally, giving rise to a rather flat top surface (Fig. S9a). These in-plane oriented pores could contribute to reduced thermal conduction in the thickness direction, while the flat top surface increased the effective surface area for sunlight absorption compared to the vertical ones, functioning similarly to the large-area leaves for transpiration. It is noted that micro-sized pores also exist on these surface cell walls (Fig. S9b), facilitating vapor escape during evaporation. These multiscale structural characteristics mimicking the whole structures of trees enabled excellent water transport, salt rejection, and thermal insulation simultaneously in SGA,

ultimately leading to highly efficient solar-powered water evaporation.

3.3 Two-Way Water and Salt Transport Mechanism in SGA

Water and salt transport are critical to the evaporation performance and efficiency. The aerogel must effectively absorb and transport water upward to the water–air interface for sustained evaporation, while avoiding salt accumulation by rejecting salt ions downward [59]. The gradient pore channels of SGA endowed a unique two-way water and salt transport mechanism mimicking the water and sugar transport in the vascular system of trees, which is more effective than common aerogels with random or vertically aligned pore channels.

To evaluate the water transport capability, we first measured the contact angles of water on the evaporation surface and the bottom surface, as shown in Figs. 3a and S10, respectively. Both surfaces showed similar contact angles of

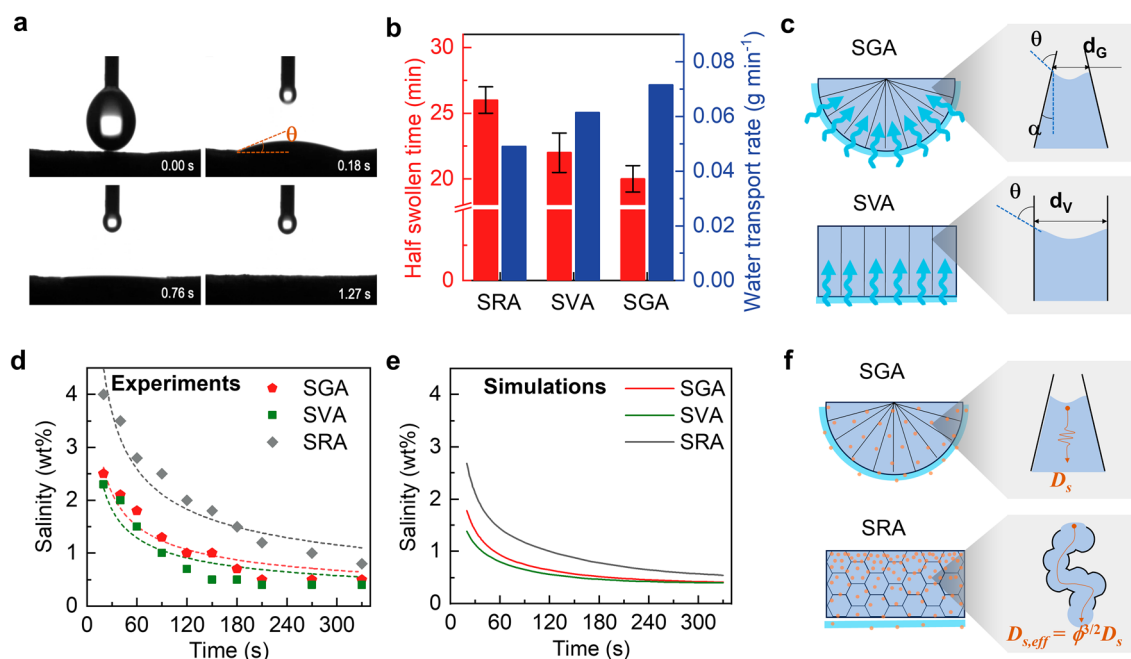


Fig. 3 Two-way water and salt transport mechanism in SGA. **a** Time-dependent contact angles of water with the surface of SGA. **b** Half swollen time and water transport rates of three structures. **c** Schematics showing the mechanisms for better water transport in SGA than SVA because of a larger surface area for water absorption and a higher capillary pressure due to tapered pore channels in the former. **d** Experimental data (solid points) fitted with Fick's second law (dash lines) and **e** simulation results for surface salinity changes of three structures as a function of time after dripping 1 mL 20 wt% brine under the isothermal condition. **f** Schematics showing the mechanism for more effective downward salt transport of SGA than SRA because of the higher effective mass diffusivity due to direct transport pathways in the former



22° when the water droplet touched the surfaces, indicating a highly hydrophilic SGA because of PVA. Moreover, the water droplet was fully absorbed within only 1.27 s thanks to the large surface area arising from the fine-root-like secondary ligaments (Fig. 2d). Further, we investigated the water transport rate of SGA by measuring the half swollen time and saturated water content using Eq. 1 [60]:

$$v = \frac{0.5}{t} \left(\frac{m_t - m_0}{m_0} \right) \quad (1)$$

where v is the water transport rate, m_t and m_0 are the masses of SGA in the initial and fully swollen states, respectively, and t is the time taken to full swelling. To highlight the advantage of the gradient pore channels in water transport, we also fabricated two other typical aerogels with random and vertical pore channels (Fig. S11), *i.e.*, structurally random aerogel (SRA) and structurally vertical aerogel (SVA), for comparison. It is noted that SRA and SVA were prepared using the same material composition and freezing temperature as SGA to maintain a uniform processing condition. As shown in Fig. 3b, the half swollen time of SGA was lower than both SRA and SVA, indicating a faster water uptake. Based on the mass changes and time, the water transport rate of SGA was 17 and 40% higher than SVA and SRA, respectively.

The best water transport properties of SGA among the three can be understood from the multiscale gradient structures, as schematically shown in Fig. 3c. Macroscopically, compared to common SRA and SVA with flat bottoms, the SGA could achieve a larger contact area for water absorption owing to the arched bottom and fan-shaped microstructures. Microscopically, the direct channels in SGA and SVA led to less resistance to water flow than the tortuous pathways in SRA, giving rise to higher water transport rates in the former. Furthermore, the water transport in SGA and SVA was driven by capillary pressures generated at the water–air interface, which were vastly different given their different pore geometries (enlarged view in Fig. 3c). The capillary pressure is given by the Young–Laplace equation:

$$\Delta p_G = \frac{4\gamma \cos(\theta - \alpha)}{d_G} \quad (2)$$

where γ is the surface tension of water, θ is the water contact angle with the channel wall, α is the angle between the cell wall and vertical direction, and d_G is the diameter of the pore channel at the meniscus. For SGA, a small d_G of 9 μm and a large α of 10° were observed from the SEM image (Fig. 2g) thanks to the tapered channels, generating a large Δp_G for

pumping the water to the evaporation surface. In comparison, the capillary pressure in SVA, Δp_v , took the same form as Eq. 2 but with $\alpha = 0^\circ$ and a large diameter, d_v , of $\sim 30 \mu\text{m}$ at the meniscus (Fig. S11a) because of the uniform diameter throughout the pore channel. Therefore, $\Delta p_G/\Delta p_v$ was calculated as 3.6, meaning 2.6 times larger capillary pressure was generated from SGA than SVA because of the gradient pore channel and smaller pore size at the meniscus of SGA. To verify the effect of pore size on water transport, we compared the water transport rates of two SVA samples with typical widths between cell walls of 10 μm (SVA-10) and 30 μm (SVA-30) prepared using different freezing temperatures of -120 and -80°C , respectively (Fig. S12a). SVA-10 showed a higher water transport rate than SVA-30 (Fig. S12b), further confirming the better water transport brought by narrower channels thanks to the higher capillary pressure. This larger capillary pressure was mainly responsible for the faster water transport in SGA than SVA with vertical channels.

In addition to upward water transport, the gradient channels in SGA also contributed to enhanced downward ion transport for salt rejection. The abilities of different structures to reject salt accumulation were compared under isothermal conditions. 1 mL brine with a concentration of 20 wt% was dripped onto the surface of SGA floating on DI water in 20 s. The salinity on the surface was measured using a refractometer (see Experimental Section for detailed salinity measurement) at different time intervals, as shown in Fig. 3d, which was compared to the other two structures. SGA and SVA showed more rapid decline in surface salinity than that of SRA, indicating faster salt transport in the former two structures, while negligible difference was noted between SGA and SVA in the salinity profiles. To understand the salt transport mechanism, the experimental data were first fitted using Fick's second law (dash lines in Fig. 3d, see detailed fitting method in Supplementary Note S2). The fittings for the three structures agreed well with the experimental data, suggesting that the downward salt transport was mainly controlled by diffusion driven by the concentration gradient. To confirm the experimental finding, we further carried out numerical simulation using a time-dependent mass diffusion-convection model coupled with incompressible flow field (see detailed numerical method in Supplementary Note S3) [44]. As shown in Fig. 3e, the simulation result agreed well with the experimental finding that SGA and SVA showed faster decays in surface salt concentration than SRA, corroborating the better downward salt transport in SGA and SVA with aligned pore channels. The salinity distributions of three structures obtained from simulations are compared in Fig.

S13. The salt distributions became almost uniform across the thickness of SGA and SVA after 120 s, while it took a longer time of 180 s for the SRA to reach equilibrium. The above experimental and simulation results substantiated the better downward salt transport performance of SGA and SVA than SRA by diffusion. The tortuous pathways of random pores in SRA generated large resistance to salt transport with a reduced effective mass diffusivity (Fig. 3f), $D_{s,\text{eff}} = \phi^{3/2} D_s$, where ϕ is the porosity and D_s is the intrinsic diffusivity of salt ions in water [4]. By contrast, the aligned channels in SGA and SVA imposed much less resistance to ion transport, leading to an effective diffusivity close to the intrinsic value. Combined with the fast upward water transport driven by the capillary pressure to replenish the evaporation surface with sufficient water, the two-way water and salt transport mechanism of SGA was expected to avoid salt accumulation for long-term solar-driven evaporation.

3.4 Simultaneous Heat Localization and Salt Rejection of SGA

In addition to fast water transport and salt rejection, effective heat localization is another critical factor contributing to a high evaporation rate and energy efficiency. However, there is often a tradeoff between excellent heat localization and salt rejection because of the highly coupled heat and mass transport in the porous evaporator [4, 44]. Although the analyses in the previous section demonstrate the effective salt rejection of SGA manifested by the unimpeded diffusion under the isothermal condition, it remains unclear if (i) simultaneous heat localization can be achieved and (ii) the diffusion can still be an effective way to reject salt when thermal effect is considered. Here, we first investigated the heat localization mechanism of SGA by quantifying different heat loss mechanisms and then probed into the salt rejection mechanism under coupled heat and mass transport.

Considering the energy balance of an evaporator, the power for evaporation (Q_{evap}) comes from the absorbed power from the sun (Q_{sun}) with some being lost to the surrounding (Q_{loss}), namely

$$Q_{\text{evap}} = Q_{\text{sun}} - Q_{\text{loss}} \quad (3)$$

Given various energy loss mechanisms, the energy balance can be expressed as [4]:

$$\begin{aligned} \dot{m}h_{LV} = & A\alpha q_{\text{solar}} - A\epsilon\sigma(T_s^4 - T_\infty^4) \\ & - Ah_a(T_s - T_\infty) - \frac{Ak_{\text{evap}}(T_s - T_\infty)}{t} \end{aligned} \quad (4)$$

The left-hand side of Eq. 4 is the power consumed for evaporation where \dot{m} is the evaporation rate (in g s^{-1}) and h_{LV} is the evaporation enthalpy of water (in J g^{-1}). The first term on the right-hand side of Eq. 4 is the power absorbed from the sun where A is the top surface area of the evaporator, α is the solar absorption, and q_{solar} is the input solar power per area. The second term represents the power of radiation loss to the ambient where ϵ is the emissivity, σ is the Stefan-Boltzmann constant. The third term describes the power of convection loss to the ambient where h_a is the convective heat transfer coefficient of air. The last term corresponds to the conduction loss to bulk water where k_{evap} is the TC and t is the thickness of evaporators.

According to the energy balance in Eq. 4 and assuming the same h_a for different structures, three thermal management strategies can be used to achieve a high evaporation rate, namely, maximizing the solar absorption (α), reducing the emissivity (ϵ), and minimizing TC (k_{evap}). The solar absorption spectra of three different structures, namely SRA, SVA, and SGA, are shown in Fig. 4a. It is noted that the absorption was measured using samples in wet states by fully saturating the three samples with water before the measurements. The wet samples aligned better with the practical evaporation condition than the dry ones. Owing to the excellent photothermal properties of GO and CNTs [61, 62], the three structures all showed high solar-weighted absorption of over 85%. Among the three, SGA showed the highest solar absorption of 93% thanks to the flat top surface arising from the in-plane cell walls, resulting in a larger effective area for sunlight absorption than both SRA and SVA. The bottom surface of SGA showed similar solar absorption (Fig. S14) compared to the top surface. In addition, the flat top surface also contributed to a reduced emissivity of SGA despite the nearly 100% emissivity of GO and CNT fillers [63]. As shown in Fig. 4b, SVA and SRA showed a high emissivity of 98.5% and 97.1%, respectively, in the mid-infrared (MIR, 3–25 μm) band because of their highly porous surface (inset of Fig. 4b). By contrast, SGA showed a reduced emissivity of 95.7% thanks to its flat surface (insets of Fig. 4b), beneficial for the low radiative heat loss. The heat loss to bulk water was mainly determined by the



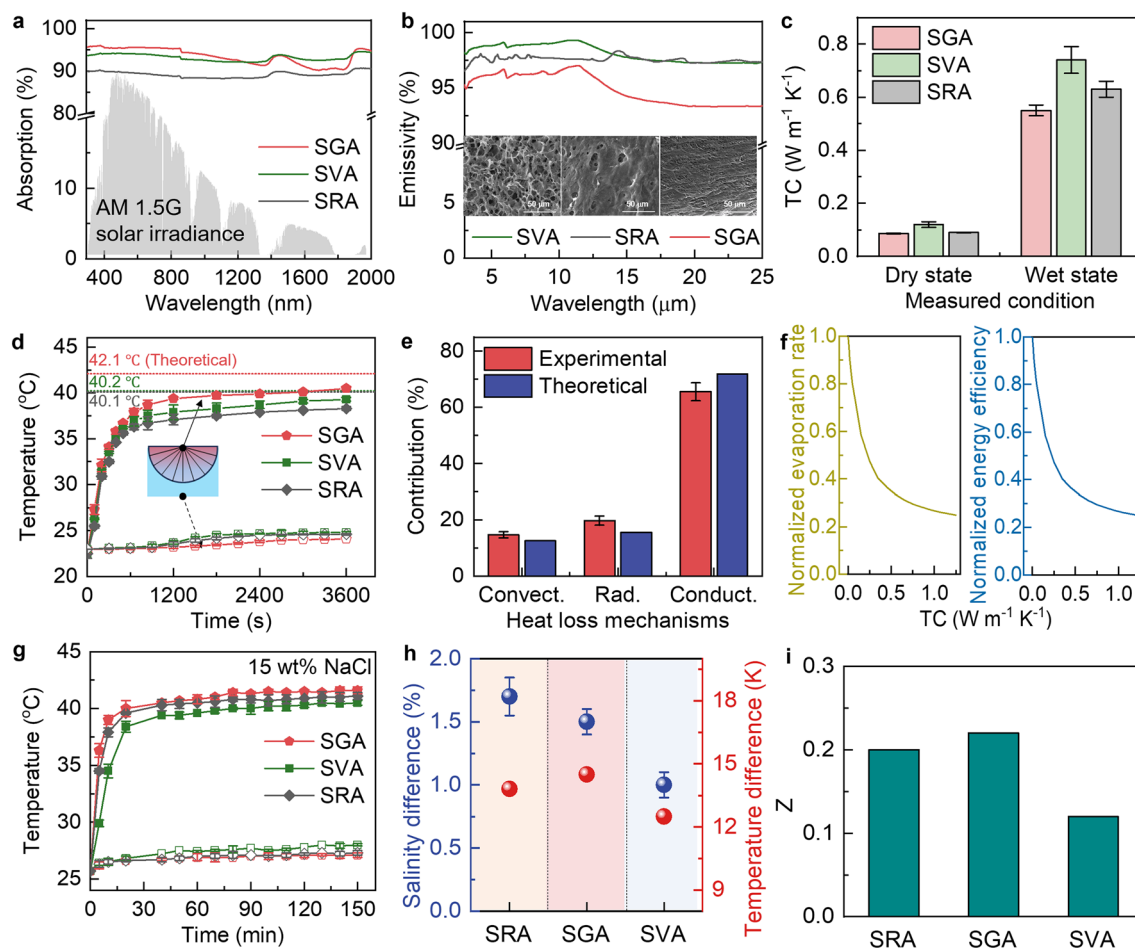


Fig. 4 Simultaneous thermal localization and salt rejection of SGA. **a** Solar absorption spectra, **b** MIR emissivity, and **c** TCs of SRA, SVA, and SGA. **d** Temperature changes of the evaporator surface (solid data point) and bulk water (hollow data point) during evaporation tests in pure water under one-sun irradiation. The dashed lines are the theoretical surface temperatures predicted from the model. **e** Contributions of different heat loss mechanisms calculated from experiments and theoretical models. **f** Effect of TC on evaporation rate and energy efficiency. **g** Temperature changes of the evaporator surface (solid data point) and bulk water (hollow data point) during evaporation tests under one-sun illumination in 15 wt% NaCl brine. **h** Temperature and salinity difference between evaporation surface and bulk water in steady-state evaporation. **i** Figure of merit, Z , of three structures calculated from Eq. 6

thermal conduction through the aerogel, warranting a low TC to mitigate the conductive heat loss. The TCs of three aerogels measured in the thickness direction are shown in Fig. 4c. In the dry state, SVA showed the highest TC of $0.12 \text{ W m}^{-1} \text{K}^{-1}$ because the vertically aligned cell walls conducted the heat effectively in the thickness direction (Fig. S11a). In comparison, SRA exhibited a lower TC of $0.09 \text{ W m}^{-1} \text{K}^{-1}$ thanks to the tortuous conductive paths created by the random pore walls (Fig. S11b). The lowest TC of $0.085 \text{ W m}^{-1} \text{K}^{-1}$ was achieved in SGA, which was 29% lower than that of SVA. After fully swelling the samples with water, SGA still maintained the lowest TC

of $0.55 \text{ W m}^{-1} \text{K}^{-1}$ among the three (Fig. 4c), even lower than that of water ($\sim 0.6 \text{ W m}^{-1} \text{K}^{-1}$). The lower TC of swollen SGA than water could be attributed to the presence of pores in SGA even when saturated [48], which was attested by its low density even in a wet state (Fig. S15). The low TC of swollen SGA contributed to the inhibited heat conduction to bulk water. The better thermal insulation performance of SGA arose from the horizontal arrangement of pore channels close to the surface, which limited the heat transport in the transverse to alignment direction and thus achieving the best insulation in the thickness direction.

The above analyses indicate that the gradient porous structure of SGA improved solar absorption while mitigating various heat loss mechanisms better than its counterparts, essential for an excellent heat localization on the evaporation surface. To evaluate the heat localization in the three structures, we monitored the temperatures of both aerogel surface and bulk water at 2 cm beneath the aerogel during evaporation tests under one-sun irradiation, as shown in Fig. 4d. For SGA, a rapid rise in surface temperature from 23 to 36 °C within 10 min was observed (red solid data points in Fig. 4d). With the increasing irradiation time, the steady-state surface temperature of SGA reached 40.6 °C, 5.7% and 9.1% higher than those of SVA and SRA, respectively. Furthermore, the temperature of bulk water beneath SGA was only elevated by 1.1 °C (red hollow data points in Fig. 4d), which was the lowest among the three structures and thus corroborated the excellent thermal localization brought by the fan-shaped pore channels.

To verify the experimental findings, we used a theoretical model with coupled heat and vapor transport to quantitatively understand the dominant heat loss mechanism and its effect on the evaporation rate. In an open system where vapor diffuses from the evaporating surface to the ambient, the evaporation rate is determined by [64]:

$$\dot{m} = M_v D_v S (c_{\text{sat}}(T_s) - \phi_{\infty} c_{\text{sat}}(T_{\infty})) \quad (5)$$

where M_v is the molar mass of vapor (in g mol⁻¹), D_v is the mass diffusivity of vapor in air (in m² s⁻¹), S is the shape factor relating to the vapor transport resistance due to evaporator geometry, ϕ_{∞} is the relative humidity at the far-field ambient, T_s and T_{∞} are the temperatures of the evaporator surface and the far-field ambient, respectively, and $c_{\text{sat}}(T_s)$ and $c_{\text{sat}}(T_{\infty})$ are the corresponding saturated vapor concentrations (in mol m⁻³). The surface temperatures of three structures in the steady state were calculated by solving Eqs. 4 and 5, shown as the dash lines in Fig. 4d (constants and parameters used in the calculation are listed in Table S1). The theoretical steady-state surface temperature of SGA is 42.1 °C, higher than that of SVA (40.2 °C) and SRA (40.1 °C), consistent with the experimental trends. To further understand the dominant heat loss mechanism in SGA, we calculated various heat loss components using the theoretical model and compared with those obtained from the experimental data, as shown in Fig. 4e (calculation details are provided in Supplementary Note S4 and Table S2). Both theoretical and experimental results suggest thermal conduction to bulk water was the major heat loss mechanism,

contributing to ~70% of the total heat loss. Since thermal conduction dominated heat loss, the lower TC of SGA than SVA and SRA was the main reason for the better heat localization. Further, we probed the effect of TC of SGA on the evaporation rate and energy efficiency using the theoretical model. The evaporation rate and energy efficiency were normalized over the values when TC was 0 (*i.e.*, the aerogel was treated as an ideal thermal insulator, see Supplementary Note S5 for details), and the effects of TC on the normalized evaporation and energy efficiency are shown in Fig. 4f. Both the evaporation rate and energy efficiency decreased parabolically with the increasing TC. When the TC was increased to 0.15 W m⁻¹ K⁻¹, the evaporation rate and energy efficiency were only ~60% that of the ideally insulated case, indicating the importance of a low TC on achieving a high evaporation rate and energy efficiency.

After revealing the excellent thermal insulation of SGA and its dominating role in heat localization for high evaporation rate and energy efficiency, we moved on to probe the salt rejection capabilities of SGA under steady-state evaporation at one-sun irradiation. Although the salt rejection of SGA under the isothermal condition (*i.e.*, no solar radiation) has been demonstrated in Sect. 3.3, it is essential to confirm the simultaneous heat localization and salt rejection under practical evaporating conditions by considering coupled heat and salt transport. The SGA was floated on a 15 wt% NaCl solution with 0.5 g solid NaCl placed on its top surface initially (Fig. S16a). Under one-sun illumination, the salt particles dissolved gradually and completely disappeared after 110 min (Fig. S16b), indicating effective salt rejection by downward salt transport through aligned pore channels in SGA under sunlight. The salt rejection mechanism of SGA can be understood as follows. Because the dynamic balance between salt accumulation rate due to evaporation and the downward ion diffusion rate determines the salt crystal nucleation on the evaporation surface, it is desired to increase downward diffusion and upward water transport simultaneously for salt rejection [19]. On the one hand, the aligned microchannels in SGA facilitated salt ion transport, leading to higher downward ion diffusivity than SRA with a random porous structure. On the other hand, the tapered microchannels in SGA induced a higher capillary pressure than those of uniform width in SVA, giving rise to faster upward water transport in the former so that sufficient water was supplied to the evaporation surface for reduced salt concentration [65]. Therefore, the two-way water and salt transport



mechanism enabled by the graded structure was responsible for the excellent salt rejection of SGA under solar irradiation.

To understand the mechanism behind simultaneous salt rejection and heat localization, we measured temperature difference, ΔT , and salinity difference, Δc , between the top of evaporation surface and bulk water to quantitatively measure thermal and salt transport, respectively. The measurements were carried out under steady-state evaporation in 15 wt% high-concentration brine and one-sun irradiation. The temperatures of the evaporation surface and bulk water for the three structures were shown in Fig. 4g. The SGA showed a higher surface temperature than SVA and SRA, whereas SVA had the highest bulk water temperature. This observation is in line with the TCs of SGA and SVA, meaning that the downward salt transport did not alter the dominant heat loss mechanism (*i.e.*, thermal conduction). The temperature and salinity differences, ΔT and Δc , between evaporation surface and bulk water of three structures are compared in Fig. 4h. In terms of thermal transport, SGA maintained the highest ΔT among the three, indicating the best heat localization on the evaporation surface. For salt transport, Δc of SVA was the smallest, indicating the best salt transport because of the vertically aligned pores to maintain a small salinity difference. On the other hand, SRA showed the largest Δc due to the random porous structure impeding the salt transport. The above analyses indicate that although SVA had a good salt rejection but lacked effective heat localization. Similarly, SRA showed decent thermal concentration while failing to reject salts. It is the fan-shaped gradient structure in SGA that enabled the simultaneous heat localization and salt rejection in the same evaporator. To quantify the material's ability to simultaneously localize heat and reject salt, we propose a figure of merit, Z , as the ratio of the amount of salt rejected, J_{salt} to the conductive heat loss, Q_{cond} [66]:

$$Z = \frac{J_{\text{salt}}}{Q_{\text{cond}}} = \left[\frac{D_{s,\text{eff}} \rho A (c_s - c_\infty)}{t} \right] / \left[\frac{A k_{\text{evap}} (T_s - T_\infty)}{t} \right] \quad (6)$$

$$= \frac{D_{s,\text{eff}} \cdot \rho \cdot \Delta c}{k_{\text{evap}} \cdot \Delta T}$$

where k_{evap} is the TC of the evaporator, $D_{s,\text{eff}}$ is the effective diffusivity of salt in the evaporator, ρ is density of salt water, and A and t are the area and thickness of the evaporator. Essentially, Z represents the amount of salt rejected per joule of heat loss. As shown in Fig. 4i, SGA attained the

highest Z value among the three structures, suggesting best salt rejection at the same heat loss. This is because the fan-shaped graded porous structure of SGA afforded both a high effective diffusivity ($D_{s,\text{eff}}$) and a low TC (k_{evap}), leading to a high Z value according to Eq. 6 for the simultaneous salt rejection and heat localization.

3.5 Solar-Powered Water Evaporation Performance

The synergistically optimized water, salt and thermal transport make the SGA an excellent candidate in solar-powered water evaporation for stable desalination. The evaporation performance of SGA was systematically studied in DI water first and was compared with SRA and SVA. The three evaporators all showed lower densities than water (Fig. S15), enabling self-floating on the water surface. The mass changes of water for different aerogel evaporators under one-sun illumination are shown in Fig. 5a. The water evaporated at the fastest rate when SGA was used as the evaporator, reaching an evaporation rate of $2.24 \text{ kg m}^{-2} \text{ h}^{-1}$ (Fig. 5b), which was 5.6 times that of pure water. Under the same irradiation, the evaporation rates of SVA and SRA were 2.03 and $1.88 \text{ kg m}^{-2} \text{ h}^{-1}$, respectively, only 69.1% and 52.7% that of the SGA. To verify the potential of SGA for practical evaporation applications, evaporation rates were further measured at different solar intensities, as shown in Fig. 5c. The evaporation rate rose with the increasing light concentration and reached as high as $6.25 \text{ kg m}^{-2} \text{ h}^{-1}$ under 5-sun irradiation. It is worth noting that even under weaker irradiation (0.5 sun), the evaporation rate was still maintained at $1.01 \text{ kg m}^{-2} \text{ h}^{-1}$, making the aerogel suitable for practical desalination under weak sunlight. The solar-to-vapor conversion efficiencies of aerogels with different structures were calculated as:

$$\eta = \frac{\dot{m} h_{LV}}{A q_{\text{solar}}} \quad (7)$$

where \dot{m} is the evaporation rate after subtracting dark evaporation, h_{LV} is the equivalent evaporation enthalpy of water (Fig. S17), A is the top surface area of the evaporator, and q_{solar} is the input solar power. As shown in Fig. 5b, The SGA achieved an energy efficiency of 85% under one sun, consistently higher than SRA (76%) and SVA (80%). According to the water and thermal transport analyses in Sects. 3.3 and 3.4, the highest evaporation rate and energy efficiency of SGA among the three structures can be attributed to the faster water transport and lower conduction loss than both SGA and SVA, substantiating the advantage of fan-shaped

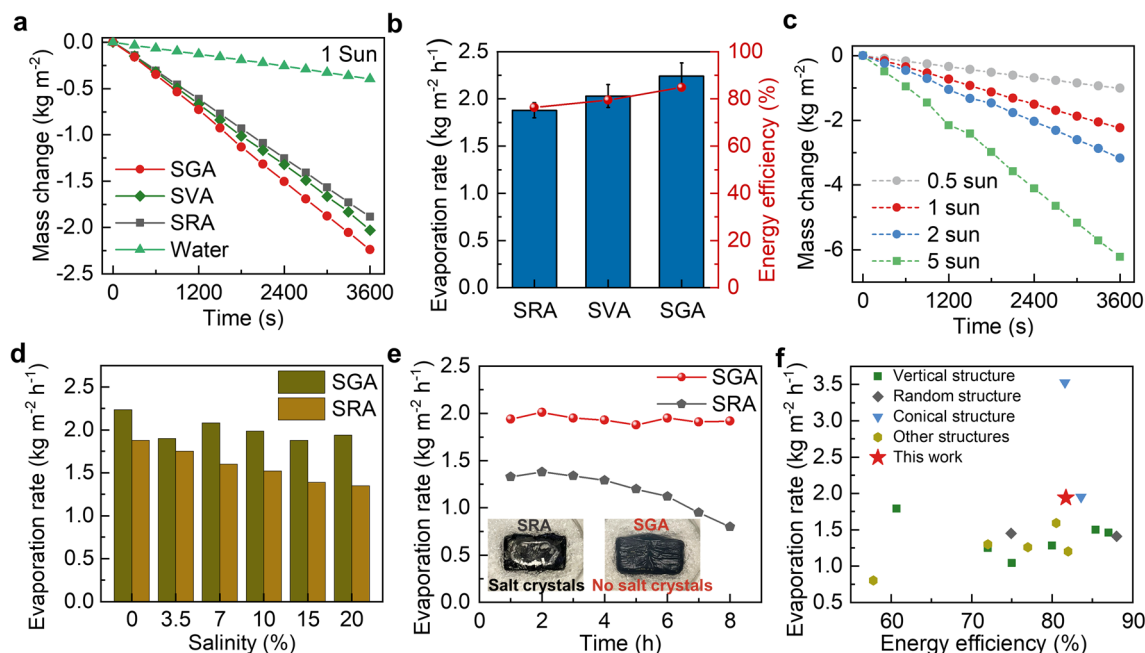


Fig. 5 Evaporation performance of SGA. **a** Mass changes of water over time under one-sun illumination when different structures are used as evaporators. **b** Evaporation rates and energy efficiencies of SRA, SVA, and SGA. **c** Mass changes of SGA under different solar intensities. **d** Evaporation rates of SGA and SRA at different salinities. **e** The changes in evaporation rates of SRA and SGA in 20 wt% brine under one-sun illumination for 8 h. Insets show the salt accumulation on the surfaces of SRA after 8-h evaporation test while no salt accumulation observed for SGA. **f** Comparison of evaporation rate and energy efficiency under 1-sun achieved using SGA with other structural evaporators in 20 wt% NaCl solution [13, 33, 34, 36, 41, 59, 68–76]

gradient structure over conventional random and vertical structures in highly efficient water generation.

In addition to the evaporation rate, avoiding salt accumulation is another key to realize efficient and stable evaporation at a high salinity because salt accumulation could lower the evaporation rate or even incapacitating the evaporator. The effective salt rejection of SGA was made possible by the two-way water and salt transport mechanism (Sect. 3.3) without degrading the heat localization (Sect. 3.4). To verify the evaporation performance under high salinity, we measured the evaporation rates of SGA and SRA in NaCl solutions with salinities ranging from 0 to 20 wt% (Fig. 5d). The evaporation rate of SRA decreased continuously from 1.88 to 1.35 $\text{kg m}^{-2} \text{h}^{-1}$ with the increasing salinity from 0 to 20 wt% because the random pores were not effective in rejecting salts at high salinities. By contrast, the evaporation rates of SGA in salt water were slightly reduced compared to that in pure water, but with no clear trend of deteriorating at high salinities. In fact, the evaporation rates in salt water remained relatively stable and reached 1.94 $\text{kg m}^{-2} \text{h}^{-1}$ even in a 20 wt% NaCl solution, indicating a negligible effect of salts on the evaporation performance. The comparison

clearly demonstrates the advantage of gradient pores to random ones in salt rejection for maintaining the evaporation performance at high salinities. To further verify the key role of the gradient structure in salt resistance, the evaporation performance of SGA was compared to SRA in a 20 wt% high-salinity brine, as shown in Fig. 5e. Unlike the consistent evaporation rate of SGA for 8 h, the evaporation rate of SRA began to decrease gradually after only 3 h of evaporation. After 8 h, the surface of SRA was completely covered by salt crystals (inset, Fig. 5e), leading to a significant drop in the evaporation rate to only 0.8 $\text{kg m}^{-2} \text{h}^{-1}$. In contrast, the evaporation rate of SGA remained stable with no salt accumulation on the evaporation surface throughout the 8-h evaporation test. Even when the evaporation test was performed continuously for 36 h, the mass change remained linear with little variation in the evaporation rate during the whole test period (Fig. S18), demonstrating the long-term stability of SGA without salt accumulation under high-salinity conditions. The above comparison signifies the positive role of the fan-shaped gradient structure in achieving simultaneous heat localization and salt rejection to maintain the excellent evaporation performance at high salinities.



Another possible factor affecting the evaporation rate and salt rejection performance is the pore channel size, which can be controlled by the freezing temperature [55]. We prepared SVA and SGA samples with different channel widths by using different freezing temperatures and compared their evaporation performance under one sun in a 20 wt% brine (see Supplementary Note S6 and Figs. S12, S19–S21 for details). We found that narrow pore channels exhibited fast evaporation at the initial stage thanks to the fast water transport due to high capillary pressures, but impeded the salt transport for deteriorated evaporation performance in the long run when salts accumulate on the evaporating surface (Figs. S19 and S21). Wide channels were preferred for avoiding salt accumulation, but they inevitably affected the heat localization, leading to low evaporation rate (Fig. S21). Therefore, a moderate channel width of $\sim 30\ \mu\text{m}$ was optimal for SGA for achieving a balance between salt rejection and heat localization.

The solar-powered evaporation performance of the SGA in the high-salinity NaCl solution (20 wt%) was compared with previously reported evaporators of different structures under the same condition (Fig. 5f). In a 20 wt% NaCl solution, the evaporation rate of SGA reached $1.94\ \text{kg m}^{-2}\ \text{h}^{-1}$. This is much higher than those vertical and random structures reported in the literature. Although a conical-structured evaporator with a wide top and narrow bottom showed better performance (blue triangles in Fig. 5f) [49], it required additional support to float on water and the preparation material was complex, which greatly reduced its feasibility for practical application. The superior evaporation performance of SGA under high-salinity conditions was attributed to its unique graded structure with fan-shaped microchannels. Although a similar vertical radiant structure was reported previously for enhanced water transport, the vertical cell walls were not able to achieve proper thermal localization [57]. Similarly, bidirectionally aligned structures provided excellent thermal insulation [67], but the upward water transport and downward salt rejection were not optimized simultaneously. Compared to these similar structures reported, the graded structure of SGA realized fast upward water transport for evaporation and downward ion transport for salt rejection at the same time while also maintaining good thermal insulation.

3.6 Practical Evaporation Performance and Stability

The practical desalination application of SGA under natural sunlight was further investigated. SGA was placed in a beaker filled with seawater, which was enclosed in a custom-made desalination setup, as shown in Fig. 6a. On a typical sunny day in Hong Kong (3 June, 2023), the setup was exposed to sunlight for 5 h (10:30 to 15:30). The changes in ambient air temperature and relative humidity are shown in Fig. 6b. The solar intensity fluctuated during the testing period with an average irradiance of $\sim 0.8\ \text{kW m}^{-2}$, continuously producing fresh water through evaporation as evidenced by the mass loss in the beaker (Fig. 6c). The total amount of water evaporated during the 5-h period was $8.86\ \text{kg m}^{-2}$, similar to the evaporation performance under the lab conditions. Moreover, the concentrations of four major ions (Na^+ , K^+ , Mg^{2+} and Ca^{2+}) in the water were reduced by two to three orders of magnitude after evaporation, fully compliant with the World Health Organization (WHO) recommended drinking water standard (Fig. 6d). Furthermore, the solar absorption spectrum of SGA after the evaporation test was similar to that before the test with no apparent degradation, suggesting no loss of GO and CNTs to water or vapor during evaporation (Fig. S22).

In addition, the long-term desalination performance of SGA was also demonstrated in a NaCl solution with a salinity of 3.5 wt% similar to the seawater. The evaporation tests were carried out for 12 h under one sun followed by exposure in the dark for another 12 h to simulate the alternation of day and night, which lasted for 7 days in total. As shown in Fig. 6e, the evaporation rates fluctuated slightly from 1.89 to $2.22\ \text{kg m}^{-2}\ \text{h}^{-1}$ during the 7-day measurements, averaging at $2.09\ \text{kg m}^{-2}\ \text{h}^{-1}$. This value was very close to the one obtained in the evaporation test of pure water, demonstrating the stable operation of SGA in seawater-like brine for a prolonged period. A continuous evaporation test in the 3.5 wt% NaCl solution was also carried out for 240 h without interruption to confirm the long-term operation stability (Fig. S23). The evaporation rate remained stable during the whole testing period, averaging at $2.05\ \text{kg m}^{-2}\ \text{h}^{-1}$. These results demonstrate the reliable long-term performance of SGA for practical solar-powered desalination and purification.

For large-scale applications, large areas of water need to be covered by SGA. Given the difficulty in producing SGA of larger sizes than a few centimeters limited by the freezing distance [46], we further demonstrated the use

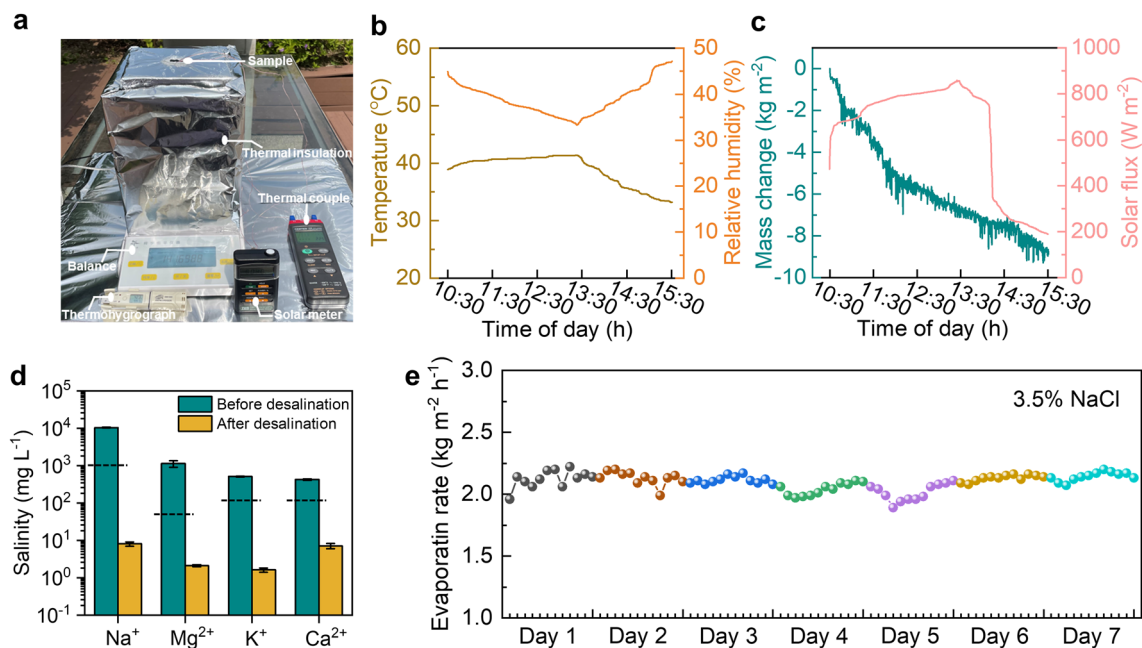


Fig. 6 Demonstration of practical water desalination and long-term stability. **a** Photograph of the outdoor test setup. **b** Air temperature, relative humidity, **c** solar flux, and accumulated mass change of water from 10:30 to 15:30 during the outdoor evaporation test. **d** The concentrations of four major ions in water before and after desalination. Black dashed lines represent the thresholds for different ions recommended by the WHO for drinking water. **e** Long-term evaporation rates of SGA in a 3.5 wt% brine under one-sun illumination

of multiple SGA floating on the water surface rather than a large piece for practical water production through solar-powered evaporation. As shown in Fig. S24a, 10 pieces of SGA covering the water surface with a total area of 20 cm² were used for water-production demonstration in a custom-made water condensation device [77]. The solar desalination setup was designed to collect fresh water through water condensation and the water collection rate was evaluated in an outdoor test. Using a transparent plastic cap as the condenser, the condensed water was collected in a beaker at the bottom (Fig. S24b). The setup was exposed to natural sunlight for 7 h during the day and the corresponding solar intensity, ambient temperature, and relative humidity are shown in Fig. S24c. During the 7-h evaporation, the freshwater collection rate calculated based on the condensed water collected in the beaker reached 1.57 kg m⁻² h⁻¹, comparable to that of previous heat-localized evaporators [78]. The clear and transparent collected water after the evaporation test (Fig. S24d) also confirmed the stability of SGA without materials leaching [79]. Considering the importance of mechanical stability of SGA in practical applications, we

measured the tensile and compressive properties of SGA (Fig. S25). The tensile stress-strain curve was measured using a hydrated sample, as shown in Fig. S25a. SGA exhibited a tensile strength of 0.33 MPa, much higher than recently reported hydrogel evaporators [80]. The compressive stress-strain curves of SGA aerogel are shown in Fig. S25b. The stress at 80% compressive strain of SGA was 8.08 MPa, which was much better than some common aerogels, such as covalent crosslinked polymer aerogels [81], MXene aerogels [82], and graphene aerogels [83]. The above analysis demonstrates the potential for large-scale application of SGA.

4 Conclusions

In summary, inspired by the water and mass transport system of trees, a multiscale structurally graded GO-CNT/PVA aerogel was developed using a radial freeze-casting technique to achieve simultaneous fast water transport, excellent salt rejection, and heat localization for highly stable solar-powered evaporation under high-salinity condition. The two-way water and salt transport mechanism

of SGA led to better water uptake and salt rejection than the vertical and random structures under isothermal conditions. In addition to fast water transport and salt rejection, effective heat localization under sunlight was simultaneously achieved in SGA by virtue of its planar surface and horizontal pore channels close to the surface. For the same amount of conductive heat loss, SGA demonstrated a larger amount of salt rejected than random and vertical structures, corroborating the unique advantage of the graded structure that allowed thermal localization and salt rejection to occur concurrently under high-salinity conditions. The synergistically fast water transport, excellent salt rejection, and heat localization empowered SGA impressive evaporation rates of $2.24 \text{ kg m}^{-2} \text{ h}^{-1}$ under one-sun illumination in DI water, which maintained stable at $1.94 \text{ kg m}^{-2} \text{ h}^{-1}$ in a 20 wt% NaCl solution without salt accumulation. Under the typical salinity of seawater, the evaporation rates also sustained consistently, averaging at $2.09 \text{ kg m}^{-2} \text{ h}^{-1}$ for 7 days without degradation. The integrated design of water, salt, and thermal transport as well as the simple preparation method developed in this work provides an enticing solution to solar-powered desalination under high-salinity conditions.

Acknowledgements This project was financially supported by the Research Grants Council of Hong Kong SAR (16200720), Environment and Conservation Fund of Hong Kong SAR (Project No. 21/2022), Young Scientists Fund of National Natural Science Foundation of China (Grant No. 52303106), Research Institute for Advanced Manufacturing (Project No. CD8R), and the start-up fund for new recruits of PolyU (Project Nos. P0038855 and P0038858). The authors appreciate the assistance from Prof. Jinglei Yang and Prof. Baoling Huang at HKUST in measuring thermal conductivity and emissivity and simulation.

Declarations

Conflict of interest The authors declare no interest conflict. They have no known competing financial interests or personal relationships that could have appeared to influence the work reported in this paper.

Open Access This article is licensed under a Creative Commons Attribution 4.0 International License, which permits use, sharing, adaptation, distribution and reproduction in any medium or format, as long as you give appropriate credit to the original author(s) and the source, provide a link to the Creative Commons licence, and indicate if changes were made. The images or other third party material in this article are included in the article's Creative Commons licence, unless indicated otherwise in a credit line to the material. If material is not included in the article's Creative Commons licence and your intended use is not permitted by statutory regulation or exceeds the permitted use, you will need to obtain

permission directly from the copyright holder. To view a copy of this licence, visit <http://creativecommons.org/licenses/by/4.0/>.

Supplementary Information The online version contains supplementary material available at <https://doi.org/10.1007/s40820-024-01448-8>.

References

1. Z. Yu, R. Gu, Y. Tian, P. Xie, B. Jin et al., Enhanced interfacial solar evaporation through formation of micro-menisci and microdroplets to reduce evaporation enthalpy. *Adv. Funct. Mater.* **32**(17), 2108586 (2022). <https://doi.org/10.1002/adfm.202108586>
2. H. Yao, P. Zhang, C. Yang, Q. Liao, X. Hao et al., Janus-interface engineering boosting solar steam towards high-efficiency water collection. *Energy Environ. Sci.* **14**(10), 5330–5338 (2021). <https://doi.org/10.1039/d1ee01381e>
3. L. Zhu, M. Gao, C.K.N. Peh, G.W. Ho, Recent progress in solar-driven interfacial water evaporation: advanced designs and applications. *Nano Energy* **57**, 507–518 (2019). <https://doi.org/10.1016/j.nanoen.2018.12.046>
4. L. Zhang, Z. Xu, L. Zhao, B. Bhatia, Y. Zhong et al., Passive, high-efficiency thermally-localized solar desalination. *Energy Environ. Sci.* **14**(4), 1771–1793 (2021). <https://doi.org/10.1039/d0ee03991h>
5. F. Zhao, Y. Guo, X. Zhou, W. Shi, G. Yu, Materials for solar-powered water evaporation. *Nat. Rev. Mater.* **5**(5), 388–401 (2020). <https://doi.org/10.1038/s41578-020-0182-4>
6. Z. Liu, Z. Zhou, N. Wu, R. Zhang, B. Zhu et al., Hierarchical photothermal fabrics with low evaporation enthalpy as heliophilic evaporators for efficient, continuous, salt-free desalination. *ACS Nano* **15**(8), 13007–13018 (2021). <https://doi.org/10.1021/acsnano.1c01900>
7. Z. Lei, X. Sun, S. Zhu, K. Dong, X. Liu et al., Nature inspired mxene-decorated 3D honeycomb-fabric architectures toward efficient water desalination and salt harvesting. *Nano-Micro Lett.* **14**(1), 10 (2021). <https://doi.org/10.1007/s40820-021-00748-7>
8. X.P. Li, X. Li, H. Li, Y. Zhao, W. Li et al., 2D ferrous ion-crosslinked $\text{Ti}_3\text{C}_2\text{T}_x$ mxene aerogel evaporators for efficient solar steam generation. *Adv. Sustain. Syst.* **5**(12), 2100263 (2021). <https://doi.org/10.1002/adsu.202100263>
9. N. Wu, Y. Yang, C. Wang, Q. Wu, F. Pan et al., Ultrathin cellulose nanofiber assisted ambient-pressure-dried, ultralight, mechanically robust, multifunctional mxene aerogels. *Adv. Mater.* **35**(1), e2207969 (2023). <https://doi.org/10.1002/adma.202207969>
10. L. Pu, H. Ma, J. Dong, C. Zhang, F. Lai et al., Xylem-inspired polyimide/mxene aerogels with radial lamellar architectures for highly sensitive strain detection and efficient solar steam generation. *Nano Lett.* **22**(11), 4560–4568 (2022). <https://doi.org/10.1021/acs.nanolett.2c01486>

11. C. Xu, M. Gao, X. Yu, J. Zhang, Y. Cheng et al., Fibrous aerogels with tunable superwettability for high-performance solar-driven interfacial evaporation. *Nano-Micro Lett.* **15**(1), 64 (2023). <https://doi.org/10.1007/s40820-023-01034-4>
12. Z. Lei, S. Zhu, X. Sun, S. Yu, X. Liu et al., A multiscale porous 3D-fabric evaporator with vertically aligned yarns enables ultra-efficient and continuous water desalination. *Adv. Funct. Mater.* **32**(40), 2205790 (2022). <https://doi.org/10.1002/adfm.202205790>
13. H. Li, W. Zhang, J. Liu, M. Sun, L. Wang et al., Self-assembled nanofibrous hydrogels with tunable porous network for highly efficient solar desalination in strong brine. *Adv. Funct. Mater.* **33**(47), 2308492 (2023). <https://doi.org/10.1002/adfm.202308492>
14. C. Xing, Z. Li, Z. Wang, S. Zhang, Z. Xie et al., Chemical scissors tailored nano-tellurium with high-entropy morphology for efficient foam-hydrogel-based solar photothermal evaporators. *Nano-Micro Lett.* **16**(1), 47 (2023). <https://doi.org/10.1007/s40820-023-01242-y>
15. C. Dang, H. Wang, Y. Cao, J. Shen, J. Zhang et al., Ultra salt-resistant solar desalination system via large-scale easy assembly of microstructural units. *Energy Environ. Sci.* **15**(12), 5405–5414 (2022). <https://doi.org/10.1039/d2ee03341k>
16. Z. Li, X. Xu, X. Sheng, P. Lin, J. Tang et al., Solar-powered sustainable water production: state-of-the-art technologies for sunlight-energy-water nexus. *ACS Nano* **15**(8), 12535–12566 (2021). <https://doi.org/10.1021/acsnano.1c01590>
17. W. Zhao, H. Gong, Y. Song, B. Li, N. Xu et al., Hierarchically designed salt-resistant solar evaporator based on donnan effect for stable and high-performance brine treatment. *Adv. Funct. Mater.* **31**(23), 2100025 (2021). <https://doi.org/10.1002/adfm.202100025>
18. L. Zhu, L. Sun, H. Zhang, H. Aslan, Y. Sun et al., A solution to break the salt barrier for high-rate sustainable solar desalination. *Energy Environ. Sci.* **14**(4), 2451–2459 (2021). <https://doi.org/10.1039/d1ee00113b>
19. G. Liu, T. Chen, J. Xu, G. Yao, J. Xie et al., Salt-rejecting solar interfacial evaporation. *Cell Rep. Phys. Sci.* **2**(1), 100310 (2021). <https://doi.org/10.1016/j.xcrp.2020.100310>
20. X. Wu, Y. Wang, P. Wu, J. Zhao, Y. Lu et al., Dual-zone photothermal evaporator for antisalt accumulation and highly efficient solar steam generation. *Adv. Funct. Mater.* **31**(34), 2102618 (2021). <https://doi.org/10.1002/adfm.202102618>
21. H. Ren, M. Tang, B. Guan, K. Wang, J. Yang et al., Hierarchical graphene foam for efficient omnidirectional solar-thermal energy conversion. *Adv. Mater.* **29**(38), 1702590 (2017). <https://doi.org/10.1002/adma.201702590>
22. Y. Xu, D. Liu, H. Xiang, S. Ren, Z. Zhu et al., Easily scaled-up photo-thermal membrane with structure-dependent auto-cleaning feature for high-efficient solar desalination. *J. Membr. Sci.* **586**, 222–230 (2019). <https://doi.org/10.1016/j.memsci.2019.05.068>
23. Y. Xia, Q. Hou, H. Jubaer, Y. Li, Y. Kang et al., Spatially isolating salt crystallisation from water evaporation for continuous solar steam generation and salt harvesting. *Energy Environ. Sci.* **12**(6), 1840–1847 (2019). <https://doi.org/10.1039/c9ee00692c>
24. Y. Wang, X. Wu, P. Wu, H. Yu, J. Zhao et al., Salt isolation from waste brine enabled by interfacial solar evaporation with zero liquid discharge. *J. Mater. Chem. A* **10**(27), 14470–14478 (2022). <https://doi.org/10.1039/d2ta03004g>
25. X. Wu, Y. Lu, X. Ren, P. Wu, D. Chu et al., Interfacial solar evaporation: from fundamental research to applications. *Adv. Mater.* e2313090 (2024). <https://doi.org/10.1002/adma.202313090>
26. T.A. Cooper, S.H. Zandavi, G.W. Ni, Y. Tsurimaki, Y. Huang et al., Contactless steam generation and superheating under one sun illumination. *Nat. Commun.* **9**(1), 5086 (2018). <https://doi.org/10.1038/s41467-018-07494-2>
27. M. Qu, Y. Zhao, J. Ge, Y. Xue, L. Mu et al., Multi-functional Janus hollow solar evaporator based on copper foam for non-contact high-efficiency solar interfacial distillation. *ACS Appl. Mater. Interfaces* **15**(30), 36999–37010 (2023). <https://doi.org/10.1021/acsaami.3c06049>
28. A.K. Menon, I. Haechler, S. Kaur, S. Lubner, R.S. Prasher, Enhanced solar evaporation using a photo-thermal umbrella for wastewater management. *Nat. Sustain.* **3**(2), 144–151 (2020). <https://doi.org/10.1038/s41893-019-0445-5>
29. W. Xu, X. Hu, S. Zhuang, Y. Wang, X. Li et al., Flexible and salt resistant Janus absorbers by electrospinning for stable and efficient solar desalination. *Adv. Energy Mater.* **8**(14), 1702884 (2018). <https://doi.org/10.1002/aenm.201702884>
30. J. Chen, J.L. Yin, B. Li, Z. Ye, D. Liu et al., Janus evaporators with self-recovering hydrophobicity for salt-rejecting interfacial solar desalination. *ACS Nano* **14**(12), 17419–17427 (2020). <https://doi.org/10.1021/acsnano.0c07677>
31. N. He, Y. Yang, H. Wang, F. Li, B. Jiang et al., Ion-transfer engineering via Janus hydrogels enables ultrahigh performance and salt-resistant solar desalination. *Adv. Mater.* **35**(24), e2300189 (2023). <https://doi.org/10.1002/adma.20230189>
32. N. He, H. Wang, H. Zhang, B. Jiang, D. Tang et al., Ionization engineering of hydrogels enables highly efficient salt-imposed solar evaporation and night-time electricity harvesting. *Nano-Micro Lett.* **16**(1), 8 (2023). <https://doi.org/10.1007/s40820-023-01215-1>
33. L. Li, N. He, B. Jiang, K. Yu, Q. Zhang et al., Highly salt-resistant 3D hydrogel evaporator for continuous solar desalination via localized crystallization. *Adv. Funct. Mater.* **31**(43), 2104380 (2021). <https://doi.org/10.1002/adfm.202104380>
34. X. Dong, Y. Si, C. Chen, B. Ding, H. Deng, Reed leaves inspired silica nanofibrous aerogels with parallel-arranged vessels for salt-resistant solar desalination. *ACS Nano* **15**(7), 12256–12266 (2021). <https://doi.org/10.1021/acsnano.1c04035>
35. W. Ma, T. Lu, W. Cao, R. Xiong, C. Huang, Bioinspired nanofibrous aerogel with vertically aligned channels for efficient water purification and salt-rejecting solar desalination. *Adv. Funct. Mater.* **33**(23), 2214157 (2023). <https://doi.org/10.1002/adfm.202214157>



36. Z.Y. Wang, Y.J. Zhu, Y.Q. Chen, H.P. Yu, Z.C. Xiong, Bioinspired aerogel with vertically ordered channels and low water evaporation enthalpy for high-efficiency salt-rejecting solar seawater desalination and wastewater purification. *Small* **19**(19), 2206917 (2023). <https://doi.org/10.1002/sml.202206917>
37. H. Zheng, J. Fan, A. Chen, X. Li, X. Xie et al., Enhancing solar-driven water purification by multiscale biomimetic evaporators featuring lamellar MoS_2/Go heterojunctions. *ACS Nano* **18**(3), 2434–2445 (2024). <https://doi.org/10.1021/acsnano.3c08648>
38. H. Liu, Z. Huang, K. Liu, X. Hu, J. Zhou, Interfacial solar-to-heat conversion for desalination. *Adv. Energy Mater.* **9**(21), 1900310 (2019). <https://doi.org/10.1002/aenm.201900310>
39. J. Yang, X. Shen, W. Yang, J.K. Kim, Templating strategies for 3D-structured thermally conductive composites: recent advances and thermal energy applications. *Prog. Mater. Sci.* **133**, 101054 (2023). <https://doi.org/10.1016/j.pmatsci.2022.101054>
40. S. He, C. Chen, Y. Kuang, R. Mi, Y. Liu et al., Nature-inspired salt resistant bimodal porous solar evaporator for efficient and stable water desalination. *Energy Environ. Sci.* **12**(5), 1558–1567 (2019). <https://doi.org/10.1039/c9ee00945k>
41. Y. Kuang, C. Chen, S. He, E.M. Hitz, Y. Wang et al., A high-performance self-regenerating solar evaporator for continuous water desalination. *Adv. Mater.* **31**(23), e1900498 (2019). <https://doi.org/10.1002/adma.201900498>
42. Y.Q. Luo, L. Liu, L.R. Zhao, J. Ju, X. Yao, Advanced solar desalination on superwetting surfaces. *J. Mater. Chem. A* **10**(37), 19348–19366 (2022). <https://doi.org/10.1039/d2ta03255d>
43. K. Sheng, M. Tian, J. Zhu, Y. Zhang, V.B. Bruggen, When coordination polymers meet wood: from molecular design toward sustainable solar desalination. *ACS Nano* **17**(16), 15482–15491 (2023). <https://doi.org/10.1021/acsnano.3c01421>
44. L. Zhang, X. Li, Y. Zhong, A. Leroy, Z. Xu et al., Highly efficient and salt rejecting solar evaporation *via* a wick-free confined water layer. *Nat. Commun.* **13**(1), 849 (2022). <https://doi.org/10.1038/s41467-022-28457-8>
45. H. Liu, C. Chen, G. Chen, Y. Kuang, X. Zhao et al., High-performance solar steam device with layered channels: Artificial tree with a reversed design. *Adv. Energy Mater.* **8**(8), 1701616 (2017). <https://doi.org/10.1002/aenm.201701616>
46. K.Y. Chan, X. Shen, J. Yang, K.T. Lin, H. Venkatesan et al., Scalable anisotropic cooling aerogels by additive freeze-casting. *Nat. Commun.* **13**(1), 5553 (2022). <https://doi.org/10.1038/s41467-022-33234-8>
47. J. Yang, K.Y. Chan, H. Venkatesan, E. Kim, M.H. Adegun et al., Superinsulating bnns/pva composite aerogels with high solar reflectance for energy-efficient buildings. *Nano-Micro Lett.* **14**(1), 54 (2022). <https://doi.org/10.1007/s40820-022-00797-6>
48. H. Zhang, X. Shen, E. Kim, M. Wang, J.H. Lee et al., Integrated water and thermal managements in bioinspired hierarchical mxene aerogels for highly efficient solar-powered water evaporation. *Adv. Funct. Mater.* **32**(19), 2111794 (2022). <https://doi.org/10.1002/adfm.202111794>
49. X. Liu, F. Chen, Y. Li, H. Jiang, D.D. Mishra et al., 3D hydrogel evaporator with vertical radiant vessels breaking the trade-off between thermal localization and salt resistance for solar desalination of high-salinity. *Adv. Mater.* **34**(36), e2203137 (2022). <https://doi.org/10.1002/adma.202203137>
50. C. Jia, Y. Li, Z. Yang, G. Chen, Y. Yao et al., Rich mesostructures derived from natural woods for solar steam generation. *Joule* **1**(3), 588–599 (2017). <https://doi.org/10.1016/j.joule.2017.09.011>
51. M. Zhu, Y. Li, G. Chen, F. Jiang, Z. Yang et al., Tree-inspired design for high-efficiency water extraction. *Adv. Mater.* **29**(44), 1704107 (2017). <https://doi.org/10.1002/adma.201704107>
52. Z. Yu, P. Wu, Biomimetic mxene-polyvinyl alcohol composite hydrogel with vertically aligned channels for highly efficient solar steam generation. *Adv. Mater. Technol.* **5**(6), 2000065 (2020). <https://doi.org/10.1002/admt.202000065>
53. Y. Kuang, C. Chen, G. Chen, Y. Pei, G. Pastel et al., Bioinspired solar-heated carbon absorbent for efficient cleanup of highly viscous crude oil. *Adv. Funct. Mater.* **29**(16), 1900162 (2019). <https://doi.org/10.1002/adfm.201900162>
54. Y. Zhuang, K. Zheng, X. Cao, Q. Fan, G. Ye et al., Flexible graphene nanocomposites with simultaneous highly anisotropic thermal and electrical conductivities prepared by engineered graphene with flat morphology. *ACS Nano* **14**(9), 11733–11742 (2020). <https://doi.org/10.1021/acsnano.0c04456>
55. E. Kim, K.Y. Chan, J. Yang, H. Venkatesan, M.H. Adegun et al., Engineering anisotropic structures of thermally insulating aerogels with high solar reflectance for energy-efficient cooling applications. *J. Mater. Chem. A* **11**(13), 7105–7114 (2023). <https://doi.org/10.1039/d2ta09983g>
56. M.H. Adegun, K.Y. Chan, J. Yang, H. Venkatesan, E. Kim et al., Anisotropic thermally superinsulating boron nitride composite aerogel for building thermal management. *Compos. Part A Appl. Sci. Manuf.* **169**, 107522 (2023). <https://doi.org/10.1016/j.compositesa.2023.107522>
57. C. Wang, X. Chen, B. Wang, M. Huang, B. Wang et al., Freeze-casting produces a graphene oxide aerogel with a radial and centrosymmetric structure. *ACS Nano* **12**(6), 5816–5825 (2018). <https://doi.org/10.1021/acsnano.8b01747>
58. W. Xu, Y. Xing, J. Liu, H. Wu, Y. Cui et al., Efficient water transport and solar steam generation *via* radially, hierarchically structured aerogels. *ACS Nano* **13**(7), 7930–7938 (2019). <https://doi.org/10.1021/acsnano.9b02331>
59. X. Chen, S. He, M.F. Mark, Y. Wang, T. Li et al., Sustainable off-grid desalination of hypersaline waters by Janus wood evaporator. *Energy Environ. Sci.* **14**(10), 5347–5357 (2021). <https://doi.org/10.1039/D1EE01505B>
60. C. Lei, J. Park, W. Guan, Y. Zhao, K.P. Johnston et al., Biomimetically assembled sponge-like hydrogels for efficient solar water purification. *Adv. Funct. Mater.* **33**(38), 2303883 (2023). <https://doi.org/10.1002/adfm.202303883>

61. B. Han, Y.L. Zhang, Q.D. Chen, H.B. Sun, Carbon-based photothermal actuators. *Adv. Funct. Mater.* **28**(40), 1802235 (2018). <https://doi.org/10.1002/adfm.201802235>
62. Z. Bao, N. Bing, H.R. Yao, Y. Zhang, H. Xie et al., Three-dimensional interpenetrating network phase-change composites with high photothermal conversion and rapid heat storage and release. *ACS Appl. Energy Mater.* **4**(8), 7710–7720 (2021). <https://doi.org/10.1021/acsam.1c01061>
63. V.D. Dao, H.S. Choi, Carbon-based sunlight absorbers in solar-driven steam generation devices. *Global Chall.* **2**(2), 1700094 (2018). <https://doi.org/10.1002/gch2.201700094>
64. G. Vaartstra, L. Zhang, Z. Lu, C.D. Díaz-Marín, J.C. Grossman et al., Capillary-fed, thin film evaporation devices. *J. Appl. Phys.* **128**(13), 130901 (2020). <https://doi.org/10.1063/5.0021674>
65. F. Nawaz, Y. Yang, S. Zhao, M. Sheng, C. Pan et al., Innovative salt-blocking technologies of photothermal materials in solar-driven interfacial desalination. *J. Mater. Chem. A* **9**(30), 16233–16254 (2021). <https://doi.org/10.1039/d1ta03610f>
66. G. Ni, S.H. Zandavi, S.M. Javid, S.V. Boriskina, T.A. Cooper et al., A salt-rejecting floating solar still for low-cost desalination. *Energy Environ. Sci.* **11**(6), 1510–1519 (2018). <https://doi.org/10.1039/c8ee00220g>
67. M. Cao, S.L. Li, J.B. Cheng, A.N. Zhang, Y.Z. Wang et al., Fully bio-based, low fire-hazard and superelastic aerogel without hazardous cross-linkers for excellent thermal insulation and oil clean-up absorption. *J. Hazard. Mater.* **403**, 123977 (2021). <https://doi.org/10.1016/j.jhazmat.2020.123977>
68. X. Dong, L. Cao, Y. Si, B. Ding, H. Deng, Cellular structured CNTs@SiO₂ nanofibrous aerogels with vertically aligned vessels for salt-resistant solar desalination. *Adv. Mater.* **32**(34), e1908269 (2020). <https://doi.org/10.1002/adma.201908269>
69. Q. Zhang, G. Yi, Z. Fu, H. Yu, S. Chen et al., Vertically aligned Janus mxene-based aerogels for solar desalination with high efficiency and salt resistance. *ACS Nano* **13**(11), 13196–13207 (2019). <https://doi.org/10.1021/acsnano.9b06180>
70. L. Song, L. Geng, Y. Tian, P. Mu, J. Li, Robust superhydrophilic attapulgite-based aligned aerogels for highly efficient and stable solar steam generation in harsh environments. *J. Mater. Chem. A* **9**(40), 23117–23126 (2021). <https://doi.org/10.1039/d1ta07042h>
71. J. He, Z. Zhang, C. Xiao, F. Liu, H. Sun et al., High-performance salt-rejecting and cost-effective superhydrophilic porous monolithic polymer foam for solar steam generation. *ACS Appl. Mater. Interfaces* **12**(14), 16308–16318 (2020). <https://doi.org/10.1021/acsami.9b22832>
72. H. Jang, J. Choi, H. Lee, S. Jeon, Corrugated wood fabricated using laser-induced graphitization for salt-resistant solar steam generation. *ACS Appl. Mater. Interfaces* **12**(27), 30320–30327 (2020). <https://doi.org/10.1021/acsami.0c05138>
73. Z. Chen, Y. Luo, Q. Li, X. Chen, Microgroove-structured PDA/PEI/PPy@PI-MS photothermal aerogel with a multilevel water transport network for highly salt-rejecting solar-driven interfacial evaporation. *ACS Appl. Mater. Interfaces* **13**(34), 40531–40542 (2021). <https://doi.org/10.1021/acsami.1c09155>
74. X. Wang, L. Zhang, D. Zheng, X. Xu, B. Bai et al., A poly-electrolyte hydrogel coated loofah sponge evaporator based on donnan effect for highly efficient solar-driven desalination. *Chem. Eng. J.* **462**, 142265 (2023). <https://doi.org/10.1016/j.cej.2023.142265>
75. M. Zou, Y. Zhang, Z. Cai, C. Li, Z. Sun et al., 3D printing a biomimetic bridge-arch solar evaporator for eliminating salt accumulation with desalination and agricultural applications. *Adv. Mater.* **33**(34), e2102443 (2021). <https://doi.org/10.1002/adma.202102443>
76. Z. Wang, Z. Zhan, Y. Li, M. Xie, H. Kong et al., A tree-root mimicked Janus evaporator for solar evaporation of saturated saline water. *J. Mater. Chem. A* **11**(48), 26592–26601 (2023). <https://doi.org/10.1039/d3ta05753d>
77. Z. Zhang, W. Xu, J. Wang, M. Hu, D. Zhang et al., Improving solar vapor generation by eliminating the boundary layer inhibition effect of evaporator pores. *ACS Energy Lett.* **8**(5), 2276–2283 (2023). <https://doi.org/10.1021/acsenerylett.3c00183>
78. M. Chen, S. Li, D. Pang, H. Yan, Selective absorber and emitter boost water evaporation and condensation toward water collection. *Mater. Today Energy* **28**, 101072 (2022). <https://doi.org/10.1016/j.mtener.2022.101072>
79. Y. Guo, Y. Sui, J. Zhang, Z. Cai, B. Xu, An all-day solar-driven vapor generator via photothermal and Joule-heating effects. *J. Mater. Chem. A* **8**(47), 25178–25186 (2020). <https://doi.org/10.1039/d0ta08329a>
80. L. Chen, Y. Wu, W. Xing, Q. Su, L. Tang et al., Mechanically robust composite hydrogels for high performance solar driven interface evaporation. *Chem. Eng. Sci.* **267**, 118330 (2023). <https://doi.org/10.1016/j.ces.2022.118330>
81. Y. Cheng, X. Zhang, Y. Qin, P. Dong, W. Yao et al., Superelasticity at 4 k of covalently crosslinked polyimide aerogels with negative poisson's ratio. *Nat. Commun.* **12**(1), 4092 (2021). <https://doi.org/10.1038/s41467-021-24388-y>
82. F. Wu, S. Qiang, X.D. Zhu, W. Jiao, L. Liu et al., Fibrous mxene aerogels with tunable pore structures for high-efficiency desalination of contaminated seawater. *Nano-Micro Lett.* **15**, 71 (2023). <https://doi.org/10.1007/s40820-023-01030-8>
83. Y.J. Wan, P.L. Zhu, S.H. Yu, R. Sun, C.P. Wong et al., Ultralight, super-elastic and volume-preserving cellulose fiber/graphene aerogel for high-performance electromagnetic interference shielding. *Carbon* **115**, 629–639 (2017). <https://doi.org/10.1016/j.carbon.2017.01.054>

